

OWT: A Foundational Organ-Wise Tokenization Framework for Medical Imaging

Sifan Song^{1*}, Siyeop Yoon^{1*}, Pengfei Jin¹, Sekeun Kim¹, Matthew Tivnan¹, Yujin Oh¹, Runqi Meng¹,
Ling Chen¹, Zhiliang Lyu¹, Dufan Wu¹, Ning Guo¹, Xiang Li^{1†}, Quanzheng Li^{1†}

¹ Center for Advanced Medical Computing and Analysis (CAMCA),
Massachusetts General Hospital and Harvard Medical School, Boston, USA

Abstract

Recent advances in representation learning often rely on holistic, black-box embeddings that entangle multiple semantic components, limiting interpretability and generalization. These issues are especially critical in medical imaging. To address these limitations, we propose an Organ-Wise Tokenization (OWT) framework with a Token Group-based Reconstruction (TGR) training paradigm. Unlike conventional approaches that produce holistic features, OWT explicitly disentangles an image into separable token groups, each corresponding to a distinct organ or semantic entity. Our design ensures each token group encapsulates organ-specific information, boosting interpretability, generalization, and efficiency while allowing fine-grained control in downstream tasks. Experiments on CT and MRI datasets demonstrate the effectiveness of OWT in not only achieving strong image reconstruction and segmentation performance, but also enabling novel semantic-level generation and retrieval applications that are out of reach for standard holistic embedding methods. These findings underscore the potential of OWT as a foundational framework for semantically disentangled representation learning, offering broad scalability and applicability to real-world medical imaging scenarios and beyond. ¹

1. Introduction

Recent years have witnessed significant advances in representation learning of visual data for both natural and medical images. The typical representation learning, driven by self-supervised and task-guided training frameworks, is classified as holistic embedding-based representation learn-

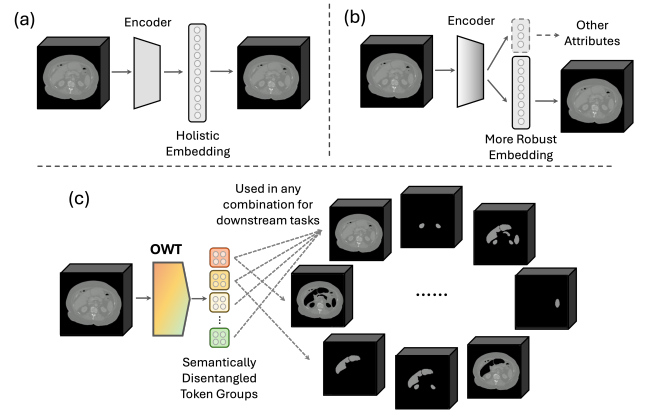


Figure 1. Objective comparison of (a) holistic embedding-based representation learning, (b) disentangled representation learning, and (c) our OWT framework. Unlike prior methods, our foundational tokenization framework enables the extraction of disentangled token groups containing semantically meaningful organ-specific representations. These token groups can be leveraged separately or in combination for downstream analyses, such as semantic-level reconstruction, segmentation, and retrieval.

ing since it learns embeddings that capture all information for an entire image [22, 54, 58] (Fig.1-a). Similar trends appear in the medical imaging domain, where holistic representations have also been extensively explored for tasks like disease diagnosis[49], organ segmentation [5, 25, 46], and anatomical structure analysis [41, 59]. Although the holistic embeddings leveraged by these studies have been proven effective, they remain globally entangled and mixed in a black-box latent space, combining information about multiple organs and background. This fusion decreases efficiency and poses significant challenges for organ-focused analyses, disease diagnosis, or radiological interpretation, where fine-grained interpretability and a semantically targeted focus are critically important [6, 48, 58].

In parallel, disentangled representation learning (DRL)

*Co-first authors.

†Corresponding authors: Contact li.quanzheng@mgh.harvard.edu

¹Code is available at <https://github.com/SifanSong/OWT>

has been studied to decompose data into semantically meaningful factors of variation, with each factor ideally corresponding to an independent aspect of the underlying data [58] (Fig. 1-b). By isolating latent factors (*e.g.*, shape, color, orientation) in natural images [4, 12, 61, 64] or modality attributes in medical images [8, 44], DRL methods aim to improve explainability and enable controllable feature manipulation. However, most conventional DRL approaches rely on purely data-driven or perturbation-driven strategies, requiring extensive modeling assumptions or specialized regularizers to ensure each factor corresponds to a semantically coherent concept [38, 58]. Consequently, existing DRL approaches face notable challenges, including limited alignment with real-world semantics, weak spatial correspondence, and poor scalability efficiency.

Despite these successes, existing holistic embedding-based strategies and DRL approaches still have notable gaps, particularly in medical imaging, where high-level interpretability and organ-specific analysis are crucial (*e.g.*, anatomical analysis and surgical planning). Specifically, existing methods suffer from **(a) a lack of interpretability and generalizability**, as multiple semantic cues are often merged without alignment to real-world concepts, making it difficult to isolate relevant structures from confounding factors (*e.g.*, background variations); and **(b) limited efficiency and controllability**, since these approaches process entire or masked representations rather than focusing only on organ-level features, restricting the ability to selectively manipulate or analyze distinct semantic factors.

These limitations motivate us to revisit the design of representation learning, aiming for explicit organ- (or part-) level tokenization to tackle them. In this paper, we propose a foundational Organ-Wise Tokenization (**OWT**) framework and a novel Token Group-based Reconstruction (**TGR**) training paradigm. Specifically, in addition to a standard encoder-decoder architecture, such as Masked Autoencoders (MAE) [27], our OWT framework incorporates two key novel modules, Organ Collector and Adaptive Holistic Embedding Restorer (**AHER**), inspired by prior structures for extracting semantic features [18, 47]. The Organ Collector integrates holistic embeddings into semantically meaningful token groups, while AHER reconstructs holistic representations from any number of token groups. Together, these modules enable a structured transition from holistic \rightarrow semantic \rightarrow holistic embeddings, facilitating both organ-specific processing and reconstruction. Meanwhile, our proposed TGR training paradigm ensures that the extracted semantic embeddings are fully functional as Semantically Disentangled Token Groups (**SDTGs**) by explicitly correlating each token group to its corresponding organ. In this case, each SDTG encapsulates only organ-specific information and is capable of being utilized independently or in any combination with other SDTGs as prac-

tically needed (Fig. 1-c).

Therefore, our design offers key advantages by addressing the limitations of existing approaches: *(i) improved interpretability and generalizability*, as each token group is explicitly associated with a specific organ or semantic content, enabling the isolation of target structures while minimizing confounding factors; and *(ii) enhanced efficiency and controllability*, as OWT processes only the relevant token groups for a given task, reducing computational load and allowing for semantic-based, fine-grained manipulation and adaptation without introducing unrelated features.

We evaluate the performance of the organ-wise embeddings (*i.e.*, SDTGs) extracted by OWT across multiple downstream tasks (such as image reconstruction, segmentation and retrieval). Across multiple modalities (CT, two MRI sequences, and a facial dataset), our method achieves better and more robust results compared to baselines (*i.e.*, MAE [27] and dedicated semantic segmentation networks [5, 9, 42, 51, 63]) and is able to accomplish tasks that these traditional methods cannot, such as semantic-level generation, retrieval and embedding combination. This proves the concept of our foundational semantically disentangled tokenization framework, enabling us to bring more potential solutions for real-world applications.

In summary, our contributions are listed as follows:

- We propose a foundational framework and a novel training paradigm, OWT and TGR, which encourage the network to encapsulate organ-level features into semantically disentangled token groups (SDTGs) rather than entangled embeddings with a black-box nature.
- The proposed SDTGs are highly condensed with rich information on each target organ, which increases the interpretability and generalization of latent embeddings.
- The token groups can be used separately or in combination and are processed with improved efficiency and controllability for downstream tasks and further analysis.
- Experiments demonstrate that our method offers significant scalability. It can adaptively integrate semantic information based on various requirements and incorporate other modalities (*e.g.*, text encoding), highlighting its potential for broader applications beyond medical imaging.

2. Related Work

2.1. Holistic Embedding-based Representation Learning

Holistic embedding-based approaches map entire 2D/3D inputs into a single latent representation, aiming to capture global image features [22, 54, 58]. These methods typically follow either self-supervised or task-guided strategies. In self-supervised learning, contrastive techniques like SimCLR [10], SimSiam [11], and BYOL [24] enforce consistency between augmented views, while predictive ap-

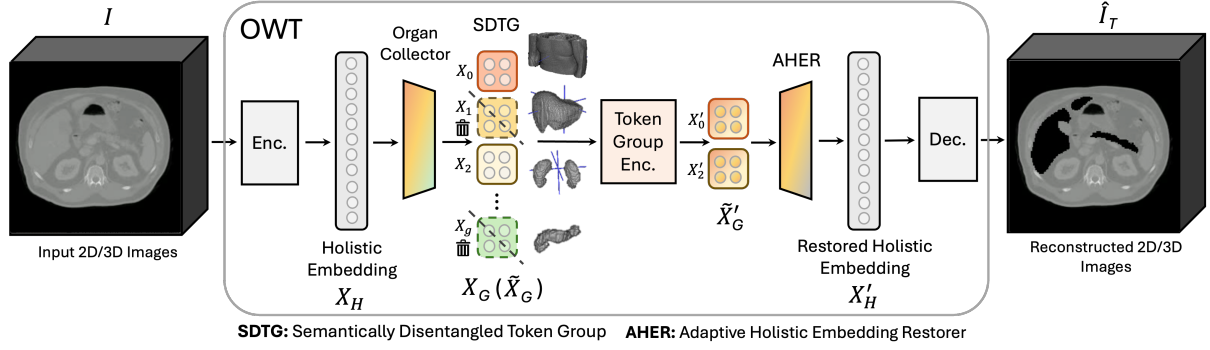


Figure 2. Overall architecture of Organ-Wise Tokenization (OWT). The input 2D or 3D images are first encoded into holistic embeddings (X_H). Then, the holistic tokens are disentangled and embedded in an organ-wise manner using the Organ Collector, forming Semantically Disentangled Token Groups (SDTGs, X_G). The SDTGs with solid lines represent randomly retained token groups (\tilde{X}_G). The Token Group Encoder further processes these retained groups, capturing both inter- and intra-organ relationships, and transforming them into \tilde{X}'_G . Finally, an Adaptive Holistic Embedding Restorer and a decoder sequentially restores the holistic representation (X'_H) and reconstructs the final output (\hat{I}_T), enabling semantic-level reconstruction.

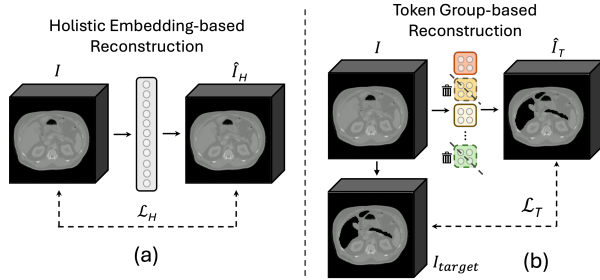


Figure 3. Comparison of the overall process of holistic embedding-based and token group-based reconstruction.

proaches such as CPC [43] and RotNet [23] reconstruct missing or permuted portions. Recently, masked image modeling (e.g., MAE [27] and BEiT [3]) has emerged as an effective approach by requiring models to infer masked regions. Meanwhile, task-guided frameworks focus on extracting features that directly benefit a target task, typically resulting in holistic embeddings. Many classic neural networks, such as ResNet [26], DenseNet [29], and Vision Transformer [16], and their variants incorporate classification, regression, or segmentation objectives.

In medical imaging, holistic representations have been widely used for self-supervised feature learning in CT [13, 32], MRI [7, 33], and X-ray [52, 60]. Additionally, classical supervised pipelines (e.g., U-Net [46] and its variants [5, 9, 25, 63]) rely on a global bottleneck to embed entire images or volumes, demonstrating strong performance in organ segmentation and disease detection. Although such approaches achieve notable success, they often encode multiple semantic factors, such as multiple organs and the surrounding background, into an entangled representation with

limited interpretability and fine-grained control [6, 48, 58].

2.2. Disentangled Representation Learning

In contrast to holistic embedding-based approaches, various disentangled representation learning (DRL) studies have pursued a dimension-wise strategy for two main objectives. First, to derive more robust holistic embeddings with improved generalizability [1, 14, 15, 20, 50, 56, 58], and second, to explicitly decompose images into latent factors, each corresponding to distinct and semantically meaningful attributes, in order to improve explainability [4, 12, 61, 64].

In medical imaging, the motivations for DRL are especially strong: improved interpretability, controllability, and robustness to confounding factors are crucial in clinical settings [37, 55]. When transitioning DRL to medical imaging, researchers seek to decouple anatomical properties (e.g., organ size or shape) [30, 57], modality characteristics (e.g., CT and MRI sequences) [8, 44], and pathological factors (e.g., tumor presence or severity) [28, 36], aiming to isolate distinct clinical features.

Despite notable progress, data- and perturbation-driven DRL approaches can be sensitive to training objectives, architecture choices, and assumptions about independent factors [38, 56, 58]. In existing studies, disentangled dimensions may not align precisely with real anatomical or pathological concepts, and spatial correspondence often remains weak when images are globally encoded. Consequently, there has been a growing emphasis on methods that combine disentanglement principles with controlled grouping or tokenization schemes to encapsulate semantically meaningful subsets of features.

3. Method

In this paper, we present a novel OWT framework and a Token Group-based Reconstruction (TGR) training paradigm, which embeds each organ into its corresponding semantically disentangled token group (SDTG). In this case, these organ-specific embeddings can be utilized independently or in combination for downstream tasks.

3.1. Overall OWT Framework

As illustrated in Fig. 2, our proposed OWT framework comprises five components: an encoder, Organ Collector, Token Group Encoder, Adaptive Holistic Embedding Restorer (AHER), and a decoder. The encoder maps input images to holistic embeddings, while the Organ Collector and TGR enable the target-organ features to be extracted and stored in specific embeddings (*i.e.*, SDTGs). In TGR, we randomly select a subset of the predefined token groups. The retained token groups are fed into the Token Group Encoder to integrate both inter-organ and intra-organ information. Next, AHER enables any number of retained token groups to be converted back into a holistic embedding. Finally, the decoder reconstructs an image of the same size as the input.

The encoder and decoder in OWT follow standard holistic representation learning architectures, so they can be Transformer-based or (fused) CNN-based, as in 2D/3D MAE [19, 27] or 2D/3D VQGAN [17, 19]. This design choice allows the framework to be applied to either 2D or 3D images with minimal modification. For a 3D input volume processed by a Transformer-based encoder, let $I \in \mathbb{R}^{D \times H \times W \times C}$. The encoder (**Enc**) produces a holistic embedding $X_H = \text{Enc}(I) \in \mathbb{R}^{(dhw) \times c_e}$, where D , H , W and C represent the depth, height, width, and channels of the volume, respectively, while d , h and w are the corresponding embedded dimensions. The (dhw) represents the number of tokens processed by the Transformer blocks, with each token having an embedding dimension of c_e . This holistic representation is then fed into subsequent modules for more fine-grained organ-wise processing.

3.2. Organ Collector

To effectively extract semantically meaningful features from the holistic embedding X_H , we introduce a novel Organ Collector module. A key component of this process is the token-wise attention matrix A_t , which dynamically assigns importance to different spatial locations or tokens, ensuring that each token group captures the most relevant semantic features.

To achieve this, let $X_H \in \mathbb{R}^{(dhw) \times c_e}$ be reshaped to $\mathbb{R}^{c_e \times d \times h \times w}$ before being fed into the Organ Collector (Fig. 2). We then employ a token-wise attention mechanism, defined as:

$$A_t = \text{Softmax}(\text{Flatten}(\alpha(X_H))) \in \mathbb{R}^{N_g \times (hw)}, \quad (1)$$

$$X_G = A_t \text{Flatten}(\gamma(X_H))^T \in \mathbb{R}^{N_g \times c_e}, \quad (2)$$

where N_g denotes the number of semantic-based tokens, and both α and γ are linear layers. Concretely, α projects the $(c_e \times d)$ -dimensional input to N_g , then applies Flatten and Softmax to derive a token-wise attention matrix. This attention matrix is multiplied by $\gamma(X_H)$ (also flattened) to obtain $X_G \in \mathbb{R}^{N_g \times c_e}$.

3.3. Token Group-based Reconstruction (TGR)

The TGR training paradigm provides direct supervision to token groups, ensuring their semantic disentanglement. By enforcing accurate organ-wise feature extraction and reconstruction through the token group-level loss \mathcal{L}_T (Fig. 3-b), TGR preserves both spatial and textural consistency. Consequently, the extracted semantic tokens serve as semantically disentangled token groups (SDTGs). Through TGR, the Organ Collector adaptively extracts organ-specific information into its corresponding SDTG, assigning each group to a particular organ.

Definition of Token Group. Given a dataset D , we have its ground-truth annotations for g organs. The remaining regions are treated as background and assigned to a single additional token group. Thus, we define a total of $(g + 1)$ token groups. Let each group contain f tokens, making the total number of tokens $N_g = (g + 1) \times f$. For example, in Fig. 2, X_0 , X_1 , and X_2 represent the token groups that store liver, kidney, and background information, respectively.

Random Selection Procedure. To manage these token groups so that they are responsible for each organ during training, we adopt a two-stage random selection procedure. **First**, randomly determine the number of retained groups: Let $\Omega \sim \mathcal{U}(0, 1)$ be a uniform random variable on $[0, 1]$. With $(g+1)$ total Token Groups, we define $\tilde{g} = \lfloor (g+1) \cdot \Omega \rfloor$, resulting in an integer $\tilde{g} \in \{0, 1, \dots, g\}$. **Second**, randomly select \tilde{g} groups: From the full set of $(g + 1)$ token groups, we then randomly pick exactly \tilde{g} groups to retain and discard the rest. We set each group to contain f tokens so that each separable and independent token group is in $\mathbb{R}^{f \times c_e}$. We concatenate the \tilde{g} selected groups along the token dimension, producing the final retained tokens $\tilde{X}_G \in \mathbb{R}^{\tilde{N}_g \times c_e}$ (Fig 2), where the final retained token count is $\tilde{N}_g = \tilde{g} \times f$.

During TGR, for each input image, we remain only areas according to randomly retain token groups based on organ annotations (Fig. 3-b), treating the processed image as the target I_{target} for the token group-based reconstruction loss \mathcal{L}_T . This explicit supervision encourages a precise organ-level focus, preserving each organ’s unique spatial and textural details in the retained token groups (*i.e.*, SDTGs). Meanwhile, any randomly excluded token groups are discarded at this stage, ensuring that only the retained groups contribute to reconstruction and thereby enhancing semantic flexibility and computational efficiency. As illustrated in Fig. 3, TGR departs from conventional holistic embedding-

Abdomen1k	Holistic-based Rec.			1 Token Group Rec.		
	L2 ↓	LPIPS ↓	SSIM-3D ↑	L2 ↓	LPIPS ↓	SSIM-3D ↑
MAE [27]	6.74e-04	0.0684	0.9688	-	-	-
MAE/LPIPS	6.19e-04	0.0403	0.9722	-	-	-
OWT	4.16e-04	0.0390	0.9734	3.31e-04	0.0073	0.9795
OWT/4slices	3.69e-04	0.0371	0.9755	2.68e-04	0.0069	0.9838

AutoPet	Holistic-based Rec.			1 Token Group Rec.		
	L2 ↓	LPIPS ↓	SSIM-3D ↑	L2 ↓	LPIPS ↓	SSIM-3D ↑
MAE [27]	2.86e-04	0.0452	0.9799	-	-	-
MAE/LPIPS	2.77e-04	0.0255	0.9843	-	-	-
OWT	1.49e-04	0.0232	0.9881	3.32e-04	0.0071	0.9778
OWT/4slices	1.13e-04	0.0179	0.9908	2.68e-04	0.0063	0.9827

Table 1. Performance of image reconstruction on CT datasets.

based reconstruction methods that rely on the latent space for the entire image [2, 17, 19, 27] (Fig. 3-a). By selectively preserving certain token groups, our approach avoids fusing diverse organ features and does not require masked tokens, resulting in improved interpretability, efficiency, and controllability during both reconstruction and subsequent tasks.

After that, we employ a Token Group Encoder (\mathbf{Enc}_G) composed of six multi-head linear self-attention blocks [31]. Let $\tilde{X}'_G = \mathbf{Enc}_G(\tilde{X}_G) \in \mathbb{R}^{\tilde{N}_g \times c_e}$ represent the further contextual modeling that captures inter- and intra-organ relationships of the retained token groups.

3.4. Adaptive Holistic Embedding Restorer

Instead of relying on conventional masked tokens, our method discards unselected token groups in the random selection procedure, simplifying training and avoiding unnecessary overhead. After the last module, each input can produce a different number of retained token groups (\tilde{X}'_G in Fig. 2), resulting in a variable token count \tilde{N}_g . To convert these tokens back into a representation aligned with the original input size (*i.e.*, the shape of the pre-Organ Collector embedding, X_H), we propose an Adaptive Holistic Embedding Restorer (AHER). This module dynamically accepts the variable token count \tilde{N}_g and restores them to a consistent dimension suitable for subsequent reconstruction.

The AHER module is also implemented using a token-wise attention mechanism, defined as:

$$A'_t = \text{Softmax}(\phi(\tilde{X}'_G)^T) \in \mathbb{R}^{(dhw) \times \tilde{N}_g}, \quad (3)$$

$$X'_H = A'_t \psi(\tilde{X}'_G) \in \mathbb{R}^{(dhw) \times c_e}, \quad (4)$$

where $\phi(\cdot)$ and $\psi(\cdot)$ are two linear transformations acting on \tilde{X}'_G , and (dhw) is the flattened spatial dimension we seek to restore (*i.e.*, the depth \times height \times width of the input volume). Specifically, a token-wise attention matrix A'_t is computed via softmax on the transposed $\phi(\tilde{X}'_G)$. Next, the features $\psi(\tilde{X}'_G)$ are re-aligned according to A'_t , yielding a restored holistic embedding X'_H (Fig. 2)

Although \tilde{N}_g varies per input, this operation preserves organ-specific features while ensuring X'_H remains a fixed

Abdomen1k	Holistic-based Rec.			1 Token Group Rec.		
	L2 ↓	LPIPS ↓	SSIM-3D ↑	L2 ↓	LPIPS ↓	SSIM-3D ↑
MAE [27]	1.37e-03	0.0465	0.9686	-	-	-
MAE/LPIPS	1.36e-03	0.0389	0.9690	-	-	-
OWT	7.65e-04	0.0256	0.9851	5.96e-04	0.0088	0.9762
OWT/4slices	5.81e-04	0.0214	0.9885	5.04e-04	0.0081	0.9801

PreArtery	Holistic-based Rec.			1 Token Group Rec.		
	L2 ↓	LPIPS ↓	SSIM-3D ↑	L2 ↓	LPIPS ↓	SSIM-3D ↑
MAE [27]	1.67e-03	0.0438	0.9701	-	-	-
MAE/LPIPS	1.74e-03	0.0375	0.9672	-	-	-
OWT	8.66e-04	0.0248	0.9851	5.29e-04	0.0089	0.9759
OWT/4slices	7.07e-04	0.0218	0.9876	4.47e-04	0.0082	0.9801

Table 2. Performance of image reconstruction on MRI datasets.

$(dhw) \times c_e$ shape, thereby maintaining consistency with the decoder. Finally, we pass X'_H through a standard decoder [27] (Dec) and unpatchify the output, reconstructing the image $\hat{I}_T = \text{Dec}(X'_H) \in \mathbb{R}^{D \times H \times W \times C}$.

As mentioned in Sec. 3.3, our objective is to reduce the discrepancy between the target image I_{target} and the reconstructed image \hat{I}_T . We combine an L2 term with the LPIPS perceptual loss [62]

$$\mathcal{L}_T = \|I_{target} - \hat{I}_T\|_2^2 + \mathcal{L}_{LPIPS}(I_{target}, \hat{I}_T) \quad (5)$$

to preserves low-level fidelity while capturing high-level perceptual similarity, thereby guiding the network to generate more realistic texture and coherent organ regions.

4. Experiments

4.1. Datasets and Experimental Setup

Datasets. We conduct experiments on four 3D medical datasets: two CT sets (Abdomen1k [40] and the CT volumes from AutoPet [21]) and two synthetic MRI sequences (delay and pre-artery) from RAOS dataset [39]. These multimodal and multi-sequence datasets validate the effectiveness and robustness of the OWT framework in medical imaging. To further validate that OWT can generalize to different semantic groupings beyond medical scenarios, we employ the CelebAMaskHQ dataset [34]. More details on the preprocessing steps are in Appendix 6.1.

Experimental Setup. All experiments are conducted on six Nvidia H100 GPUs. The hyperparameters, optimizer and scheduler settings follow MAE [27]. We compare OWT against a baseline MAE due to the similar encoder-decoder structure. In OWT, the default token number for each token group is 20. For processing 3D volumes (4 slices by default), we adopt a 3D version of MAE [19]. For fairness, we add LPIPS loss [62] to MAE to improve reconstruction quality. We also explore replacing the encoder-decoder pair with that of VQGAN [17]. Further details of architectures and hyperparameters are in Appendices 6.2 and 6.3, and ablation studies of default settings are in Appendix 8.

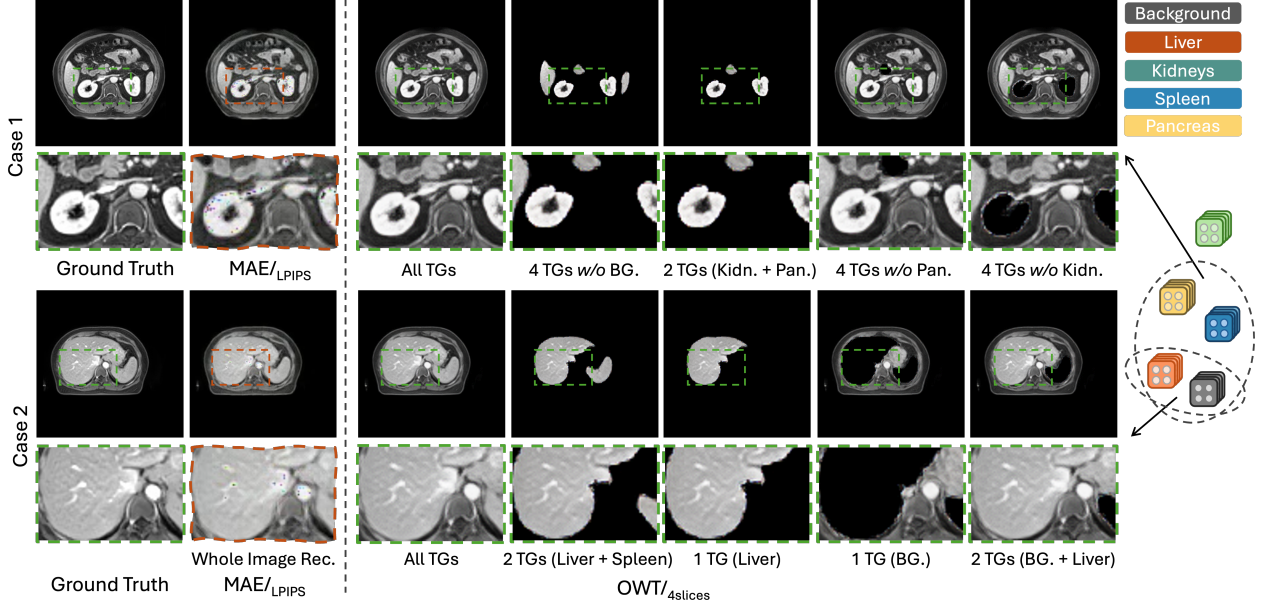


Figure 4. Samples of holistic-based and semantic-based medical image reconstruction from an MRI dataset.

4.2. Results

Our OWT framework not only yields highly condensed representations containing rich information but also provides semantically meaningful and disentangled token groups. In this section, we design extensive experiments to evaluate OWT’s performance on several downstream tasks, including reconstruction, segmentation, generalization, and retrieval (Sec. 4.2.1). Notably, our findings indicate that, in contrast to conventional holistic-based methods, OWT can focus on semantic-level tasks and analyses, delivering superior interpretability and controllability. Next, we investigate the characteristics of these semantically disentangled token groups and explore their potential to incorporate other modalities (Sec. 4.2.2). We then demonstrate that the OWT framework can be employed in real-world applications (Sec. 4.2.3). Additionally, we provide ablation studies and explore more architectures of the OWT framework in Appendix 8.

4.2.1. Downstream Analysis

Image Reconstruction. We evaluate the reconstruction capability of OWT across four datasets (two CT and two MRI) [21, 39, 40]. Tables 1 and 2 show that OWT outperforms MAE on L2, LPIPS, and 3D SSIM metrics in holistic-based reconstruction tasks. Moreover, leveraging a patch-embedding module that tokenizes four slices for 3D volumes generates better results than the 2D OWT variant.

We further explore a semantic-based reconstruction scenario by retaining only a single organ-wise token group at a time, feeding it through AHER and the decoder to generate

Methods	CT		MRI	
	Abdomen1k	AutoPet	Delay	PreArtery
UNetplus [63]	88.38	89.29	84.11	84.42
AttU_Net [42]	89.34	89.73	84.54	85.04
TransUnet [9]	88.91	89.70	84.97	84.29
Swin-Unet [5]	86.56	88.06	83.07	82.41
CMUNet [51]	88.33	89.48	84.82	85.56
OWT	89.30	89.52	85.85	85.67
OWT/ _{4slices}	91.37_{+2.03}	91.41_{+1.68}	87.72_{+1.87}	87.31_{+1.64}

Table 3. Performance of semantic segmentation.

an organ-specific image. As reported in Tables 1 and 2, using a larger number of slices in CT and MRI volumes leads to more robust disentangled token groups, thereby improving semantic-based reconstruction quality. Fig. 4 illustrates MRI cases (rich in textural detail). Even with LPIPS added, MAE suffers from noticeable detail loss, whereas OWT (all token groups retained) produces sharper and clearer details. Additionally, we can freely combine the token groups to reconstruct only the content of interest.

In the zoom-in rows of Fig. 4, the liver/kidney reconstruction appears nearly identical whether we use only the liver/kidney token group or combine it with others, suggesting that OWT’s organ token groups are highly semantically independent. This property offers better interpretability as well as controllability, enabling reconstruction without unnecessary entanglement of unrelated organ features.

Image Segmentation. We observe that reconstructing token groups with OWT preserves clear spatial details and boundary information in Fig. 4. Consequently, a simple thresholding operation on the predictions can gener-

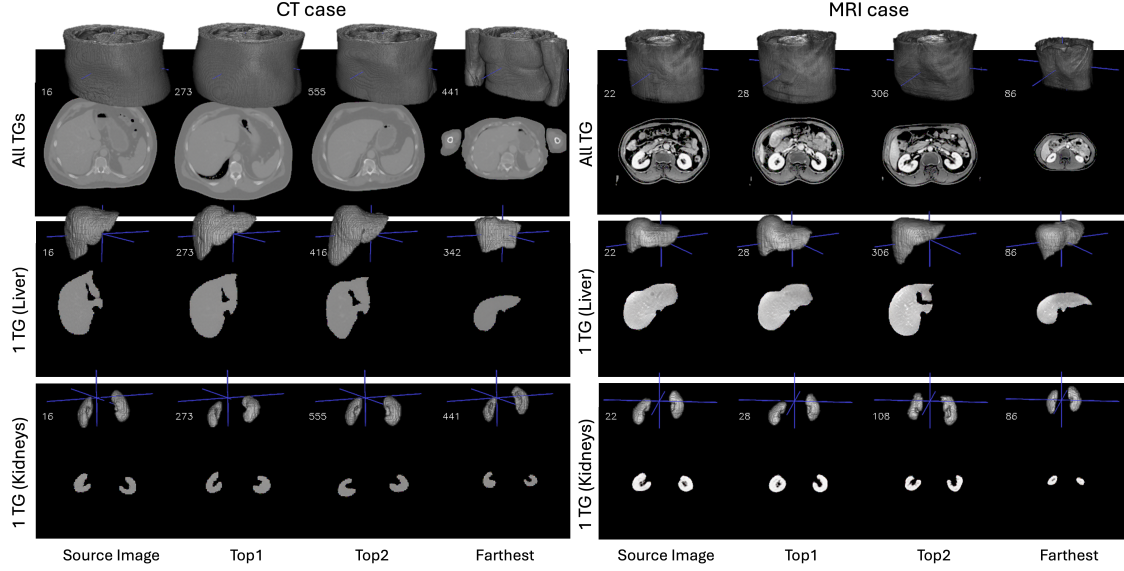


Figure 5. Semantic-based retrieval of CT/MRI images.

AutoPet	Holistic-based Rec.		1 Token Group Rec.		1 Token Group Seg.
	$L_2 \downarrow$	SSIM-3D \uparrow	$L_2 \downarrow$	SSIM-3D \uparrow	Dice \uparrow
MAE/ L_{PIPS} [27]	3.58e-04	0.9872	-	-	-
AttU_Net [42]	-	-	-	-	87.03
CMUNet [51]	-	-	-	-	87.89
OWT	1.12e-04	0.9909	4.07e-04	0.9765	87.54
OWT/ $_{4slices}$	9.34e-05	0.9924	3.60e-04	0.9798	89.42

Table 4. Generalization capability of cross-dataset experiments trained on Abdomen1k and tested on AutoPet.

ate semantic binary masks, offering direct evidence of each organ-wise token group’s independence and interpretability. Table 3 reports the single-organ segmentation Dice scores (averaged over the liver, kidneys, spleen, and pancreas). Overall, the accuracy of OWT’s organ-specific reconstructions is comparable to that of several dedicated 2D segmentation networks. Moreover, incorporating information from adjacent slices (OWT/ $_{4slices}$) further improves performance, surpassing the second-best approach by an average margin of 1.805 across four CT and MRI datasets (green number in Table 3). The detailed Dice of each organ are in Appendix 7.

Generalization. Table 4 reports the generalization performance when all methods are trained on Abdomen1k and tested on the AutoPet dataset. Under both reconstruction and segmentation metrics, OWT/ $_{4slices}$ outperforms dedicated holistic-based approaches. Moreover, it also achieves strong results in single-organ reconstruction, indicating that token groups can be flexibly combined or used individually to mitigate interference from irrelevant organs and background regions. Consequently, the semantic features extracted by OWT generalize more effectively, underscoring its potential as a foundational tokenization framework.

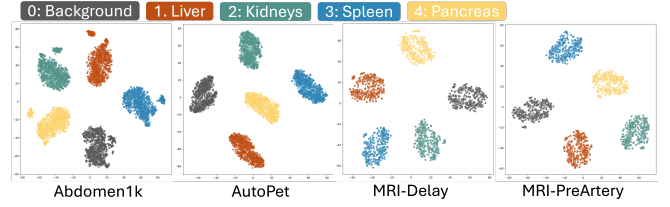


Figure 6. t-SNE visualization of independent token groups on four medical datasets.

4.2.2. Look Deeper into Token Groups

Semantic Information in Token Groups. Fig. 6 illustrates the t-SNE results of how the Organ Collector (with TGR) embeds the background and four organs into the latent space (*i.e.*, five token groups) for each dataset. Within this space, token vectors of the same group type exhibit dense clusters, whereas different token groups remain distinctly separated. This clear inter-group separation highlights the semantic independence of organ-specific token groups in OWT, indicating strong potential for downstream tasks.

Due to the semantic independence of the token group, Fig. 5 shows that our approach not only supports holistic-level retrieval, but also enables organ-level retrieval (L_2 distance measure). Specifically, we demonstrate top-1, top-2, and maximum-distance retrieval results on both CT and MRI modalities for different token groups. The case indices in the top-left corner of each row indicate how retrieval results vary for different organs of interest. Since experiments in reconstruction and segmentation demonstrate that each token group preserves both the spatial structure and texture details of its corresponding organ, this organ-specific

AutoPet	Holistic-based Rec.		1 Token Group Rec.	
	L2 ↓	LPIPS ↓	L2 ↓	LPIPS ↓
OWT	1.49e-04	0.0232	3.32e-04	0.0071
OWT w/ Text	1.41e-04	0.0221	3.16e-04	0.0068

Table 5. Reconstruction comparison between OWT w/ and w/o incorporated text prompts.

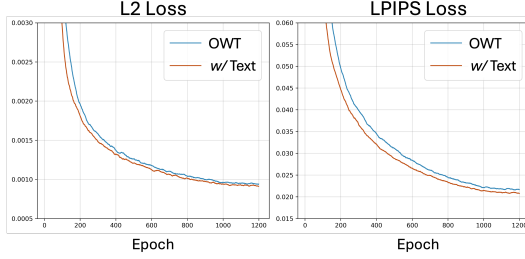


Figure 7. Loss comparison between OWT w/ and w/o incorporated text prompts.

CelebAMaskHQ	Holistic-based Rec.		1 Token Group Rec.	
	L2 ↓	LPIPS ↓	L2 ↓	LPIPS ↓
MAE/LPIPS [27]	2.78e-03	0.1157	-	-
OWT	2.50e-03	0.1101	2.83e-03	0.0458

Table 6. Performance of OWT on CelebAMaskHQ dataset.

retrieval can be highly beneficial in medical scenarios. For example, it can help radiologists quickly locate similar organ regions across multiple patients, facilitate region-based comparisons of pathology progression, or assist in reference image selection for organ-specific diagnoses.

Multi-Modality Incorporation. In OWT, each organ is embedded into its corresponding SDTG, resulting in highly semantically disentangled and independent representations. Therefore, these representations can be efficiently aligned with or collaborated on with other modality embeddings (*e.g.*, text encoding). Specifically, during OWT training, we use medical prompts and a pretrained CLIP encoder [45] to obtain text encoding of each organ, which are then added element-wise to their matching token groups after the Organ Collector. (More details on prompts and architecture for training OWT w/ text encoding are in Appendix 6.2.2.)

Fig. 7 and Table 5 reveal that simply adding text prompts to organ-wise token groups instantly accelerates loss convergence and provides slight improvements in both holistic- and semantic-based reconstruction. Consequently, OWT shows promise for incorporating the text modality to further enhance organ-specific representations. Such multi-modal integration could unlock new medical applications, such as more robust organ labeling, guided retrieval and generation, and improved interpretability in complex workflows.

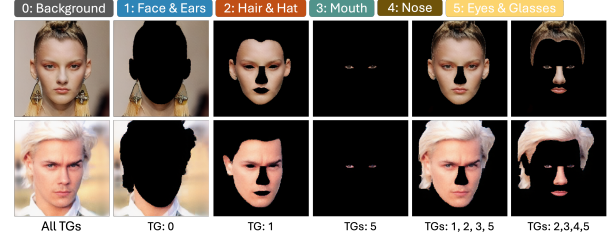


Figure 8. Samples of holistic-based and semantic-based human face reconstruction on CelebAMaskHQ.

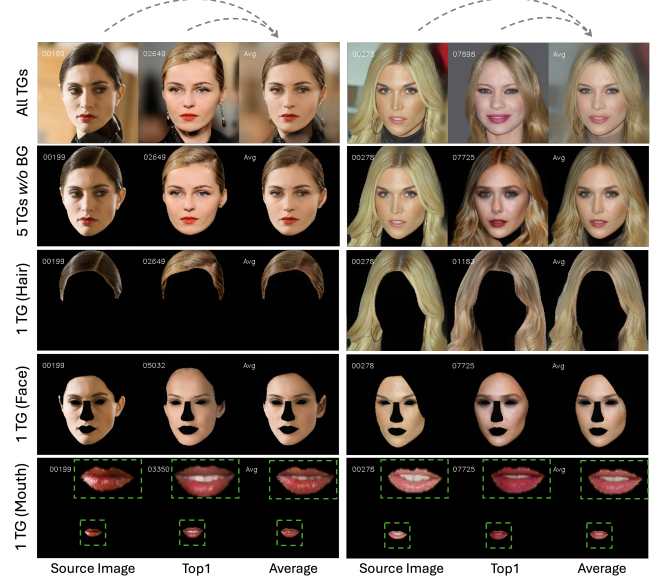


Figure 9. Semantic-based retrieval of CelebAMaskHQ.

4.2.3. Organ-wise Token Groups are more than Organs

Although OWT and TGR are primarily designed for grouping different semantic components in medical images, they can also be applied to non-medical datasets. As a proof of concept, we demonstrate in Fig. 8 and Table 6 that OWT successfully learns semantically disentangled token groups on the CelebAMaskHQ dataset, capturing and reconstructing each facial region with high spatial and textural fidelity.

As illustrated in Fig. 9, each token group facilitates semantic-based retrieval for different facial attributes (*e.g.*, hair, skin, lips). In the third column, we conduct an experiment by averaging source token group(s) with the Top1 retrieved token group(s). Notably, this averaged token group(s) can still be reconstructed, exhibiting features that blend and transition between both identities (*e.g.*, overall facial attributes, hair color, skin tone, lip color, mouth openness). These observations imply that token groups extracted by OWT can enable fine-grained editing or hybrid generation of facial attributes without background influence, offering enhanced interpretability, efficiency, and controllability.

5. Conclusion

In this paper, we propose a novel Organ-Wise Tokenization (OWT) framework and Token Group-Based Reconstruction (TGR) paradigm, which disentangle holistic embeddings into semantically disentangled token groups. Our approach not only improves interpretability, generalizability, efficiency and controllability in organ-based analyses, but also shows adaptability to broader scenarios, including natural image domains. By enabling semantic-level token groups, OWT enriches downstream tasks such as semantic-based reconstruction, segmentation and retrieval, offering a new perspective on how representations can be leveraged.

References

- [1] Gairui Bai, Wei Xi, Xiaopeng Hong, Xinhui Liu, Yang Yue, and Songwen Zhao. Robust and rotation-equivariant contrastive learning. *IEEE Transactions on Neural Networks and Learning Systems*, 2023. 3
- [2] Dor Bank, Noam Koenigstein, and Raja Giryes. Autoencoders. *Machine learning for data science handbook: data mining and knowledge discovery handbook*, pages 353–374, 2023. 5
- [3] Hangbo Bao, Li Dong, Songhao Piao, and Furu Wei. Beit: Bert pre-training of image transformers. *arXiv preprint arXiv:2106.08254*, 2021. 3
- [4] Christopher P Burgess, Irina Higgins, Arka Pal, Loic Matthey, Nick Watters, Guillaume Desjardins, and Alexander Lerchner. Understanding disentangling in beta-vae. *arXiv preprint arXiv:1804.03599*, 2018. 2, 3
- [5] Hu Cao, Yueyue Wang, Joy Chen, Dongsheng Jiang, Xiaopeng Zhang, Qi Tian, and Manning Wang. Swin-unet: Unet-like pure transformer for medical image segmentation. In *European conference on computer vision*, pages 205–218. Springer, 2022. 1, 2, 3, 6
- [6] Irem Cetin, Maialen Stephens, Oscar Camara, and Miguel A González Ballester. Attri-vae: Attribute-based interpretable representations of medical images with variational autoencoders. *Computerized Medical Imaging and Graphics*, 104:102158, 2023. 1, 3
- [7] Krishna Chaitanya, Ertunc Erdil, Neerav Karani, and Ender Konukoglu. Contrastive learning of global and local features for medical image segmentation with limited annotations. *Advances in neural information processing systems*, 33:12546–12558, 2020. 3
- [8] Agisilaos Chartsias, Thomas Joyce, Giorgos Papanastasiou, Scott Semple, Michelle Williams, David E Newby, Rohan Dharmakumar, and Sotirios A Tsafaris. Disentangled representation learning in cardiac image analysis. *Medical image analysis*, 58:101535, 2019. 2, 3
- [9] Jieneng Chen, Yongyi Lu, Qihang Yu, Xiangde Luo, Ehsan Adeli, Yan Wang, Le Lu, Alan L Yuille, and Yuyin Zhou. Transunet: Transformers make strong encoders for medical image segmentation. *arXiv preprint arXiv:2102.04306*, 2021. 2, 3, 6
- [10] Ting Chen, Simon Kornblith, Mohammad Norouzi, and Geoffrey Hinton. A simple framework for contrastive learning of visual representations. In *International conference on machine learning*, pages 1597–1607. PmLR, 2020. 2
- [11] Xinlei Chen and Kaiming He. Exploring simple siamese representation learning. In *Proceedings of the IEEE/CVF conference on computer vision and pattern recognition*, pages 15750–15758, 2021. 2
- [12] Xi Chen, Yan Duan, Rein Houthoofd, John Schulman, Ilya Sutskever, and Pieter Abbeel. Infogan: Interpretable representation learning by information maximizing generative adversarial nets. *Advances in neural information processing systems*, 29, 2016. 2, 3
- [13] Xiaocong Chen, Lina Yao, Tao Zhou, Jinming Dong, and Yu Zhang. Momentum contrastive learning for few-shot covid-19 diagnosis from chest ct images. *Pattern recognition*, 113: 107826, 2021. 3
- [14] Rumen Dangovski, Li Jing, Charlotte Loh, Seungwook Han, Akash Srivastava, Brian Cheung, Pulkit Agrawal, and Marin Soljačić. Equivariant contrastive learning. *arXiv preprint arXiv:2111.00899*, 2021. 3
- [15] Alexandre Devillers and Mathieu Lefort. Equimod: An equivariance module to improve visual instance discrimination. In *International Conference on Learning Representations*, 2023. 3
- [16] Alexey Dosovitskiy, Lucas Beyer, Alexander Kolesnikov, Dirk Weissenborn, Xiaohua Zhai, Thomas Unterthiner, Mostafa Dehghani, Matthias Minderer, Georg Heigold, Sylvain Gelly, et al. An image is worth 16x16 words: Transformers for image recognition at scale. *arXiv preprint arXiv:2010.11929*, 2020. 3
- [17] Patrick Esser, Robin Rombach, and Bjorn Ommer. Taming transformers for high-resolution image synthesis. In *Proceedings of the IEEE/CVF conference on computer vision and pattern recognition*, pages 12873–12883, 2021. 4, 5
- [18] Mohsen Fayyaz, Soroush Abbasi Koohpayegani, Farnoush Rezaei Jafari, Sunando Sengupta, Hamid Reza Vaezi Joze, Eric Sommerlade, Hamed Pirsiavash, and Jürgen Gall. Adaptive token sampling for efficient vision transformers. In *European Conference on Computer Vision*, pages 396–414. Springer, 2022. 2
- [19] Christoph Feichtenhofer, Yanghao Li, Kaiming He, et al. Masked autoencoders as spatiotemporal learners. *Advances in neural information processing systems*, 35:35946–35958, 2022. 4, 5
- [20] Quentin Garrido, Laurent Najman, and Yann Lecun. Self-supervised learning of split invariant equivariant representations. *arXiv preprint arXiv:2302.10283*, 2023. 3
- [21] S. Gatidis and T. Kuestner. A whole-body fdg-pet/ct dataset with manually annotated tumor lesions (fdg-pet-ct-lesions). Dataset, 2022. 5, 6, 1
- [22] Robert Geirhos, Jörn-Henrik Jacobsen, Claudio Michaelis, Richard Zemel, Wieland Brendel, Matthias Bethge, and Felix A Wichmann. Shortcut learning in deep neural networks. *Nature Machine Intelligence*, 2(11):665–673, 2020. 1, 2
- [23] Spyros Gidaris, Praveer Singh, and Nikos Komodakis. Unsupervised representation learning by predicting image rotations. *arXiv preprint arXiv:1803.07728*, 2018. 3
- [24] Jean-Bastien Grill, Florian Strub, Florent Altché, Corentin Tallec, Pierre Richemond, Elena Buchatskaya, Carl Doersch,

- Bernardo Avila Pires, Zhaoan Guo, Mohammad Gheshlaghi Azar, et al. Bootstrap your own latent-a new approach to self-supervised learning. *Advances in neural information processing systems*, 33:21271–21284, 2020. 2
- [25] Ali Hatamizadeh, Vishwesh Nath, Yucheng Tang, Dong Yang, Holger R Roth, and Daguang Xu. Swin unetr: Swin transformers for semantic segmentation of brain tumors in mri images. In *International MICCAI brainlesion workshop*, pages 272–284. Springer, 2021. 1, 3
- [26] Kaiming He, Xiangyu Zhang, Shaoqing Ren, and Jian Sun. Deep residual learning for image recognition. In *Proceedings of the IEEE conference on computer vision and pattern recognition*, pages 770–778, 2016. 3
- [27] Kaiming He, Xinlei Chen, Saining Xie, Yanghao Li, Piotr Dollár, and Ross Girshick. Masked autoencoders are scalable vision learners. In *Proceedings of the IEEE/CVF conference on computer vision and pattern recognition*, pages 16000–16009, 2022. 2, 3, 4, 5, 7, 8
- [28] Anjun Hu, Jean-Pierre R Falet, Brennan S Nichyporuk, Changjian Shui, Douglas L Arnold, Sotirios A Tsaftaris, and Tal Arbel. Clinically plausible pathology-anatomy disentanglement in patient brain mri with structured variational priors. *arXiv preprint arXiv:2211.07820*, 2022. 3
- [29] Gao Huang, Zhuang Liu, Laurens Van Der Maaten, and Kilian Q Weinberger. Densely connected convolutional networks. In *Proceedings of the IEEE conference on computer vision and pattern recognition*, pages 4700–4708, 2017. 3
- [30] Kaida Jiang, Li Quan, and Tao Gong. Disentangled representation and cross-modality image translation based unsupervised domain adaptation method for abdominal organ segmentation. *International Journal of Computer Assisted Radiology and Surgery*, 17(6):1101–1113, 2022. 3
- [31] Angelos Katharopoulos, Apoorv Vyas, Nikolaos Pappas, and François Fleuret. Transformers are rnns: Fast autoregressive transformers with linear attention. In *International conference on machine learning*, pages 5156–5165. PMLR, 2020. 5, 1
- [32] Haoran Lai, Zihang Jiang, Qingsong Yao, Rongsheng Wang, Zhiyang He, Xiaodong Tao, Wei Wei, Weifu Lv, and S Kevin Zhou. E3d-gpt: Enhanced 3d visual foundation for medical vision-language model. *arXiv preprint arXiv:2410.14200*, 2024. 3
- [33] Daniel M Lang, Eli Schwartz, Cosmin I Bercea, Raja Giryes, and Julia A Schnabel. 3d masked autoencoders with application to anomaly detection in non-contrast enhanced breast mri. *arXiv preprint arXiv:2303.05861*, 2023. 3
- [34] Cheng-Han Lee, Ziwei Liu, Lingyun Wu, and Ping Luo. Maskgan: Towards diverse and interactive facial image manipulation. In *Proceedings of the IEEE/CVF conference on computer vision and pattern recognition*, pages 5549–5558, 2020. 5, 1
- [35] Jie Liu, Yixiao Zhang, Jie-Neng Chen, Junfei Xiao, Yongyi Lu, Bennett A Landman, Yixuan Yuan, Alan Yuille, Yucheng Tang, and Zongwei Zhou. Clip-driven universal model for organ segmentation and tumor detection. In *Proceedings of the IEEE/CVF international conference on computer vision*, pages 21152–21164, 2023. 1
- [36] Tianling Liu, Wennan Liu, Lequan Yu, Liang Wan, Tong Han, and Lei Zhu. Joint prediction of meningioma grade and brain invasion via task-aware contrastive learning. In *International Conference on Medical Image Computing and Computer-Assisted Intervention*, pages 355–365. Springer, 2022. 3
- [37] Xiao Liu, Pedro Sanchez, Spyridon Thermos, Alison Q O’Neil, and Sotirios A Tsaftaris. Learning disentangled representations in the imaging domain. *Medical Image Analysis*, 80:102516, 2022. 3
- [38] Francesco Locatello, Stefan Bauer, Mario Lucic, Gunnar Raetsch, Sylvain Gelly, Bernhard Schölkopf, and Olivier Bachem. Challenging common assumptions in the unsupervised learning of disentangled representations. In *international conference on machine learning*, pages 4114–4124. PMLR, 2019. 2, 3
- [39] Xiangde Luo, Zihan Li, Shaoting Zhang, Wenjun Liao, and Guotai Wang. Rethinking abdominal organ segmentation (raos) in the clinical scenario: A robustness evaluation benchmark with challenging cases. In *International Conference on Medical Image Computing and Computer-Assisted Intervention*, pages 531–541. Springer, 2024. 5, 6, 1
- [40] Jun Ma, Yao Zhang, Song Gu, Cheng Zhu, Cheng Ge, Yichi Zhang, Xingle An, Congcong Wang, Qiyuan Wang, Xin Liu, et al. Abdomenct-1k: Is abdominal organ segmentation a solved problem? *IEEE Transactions on Pattern Analysis and Machine Intelligence*, 44(10):6695–6714, 2021. 5, 6, 1
- [41] MHD Jafar Mortada, Selene Tomassini, Haidar Anbar, Micaela Morettini, Laura Burattini, and Agnese Sbrollini. Segmentation of anatomical structures of the left heart from echocardiographic images using deep learning. *Diagnostics*, 13(10):1683, 2023. 1
- [42] Ozan Oktay, Jo Schlemper, Loic Le Folgoc, Matthew Lee, Mattias Heinrich, Kazunari Misawa, Kensaku Mori, Steven McDonagh, Nils Y Hammerla, Bernhard Kainz, et al. Attention u-net: Learning where to look for the pancreas. *arXiv preprint arXiv:1804.03999*, 2018. 2, 6, 7
- [43] Aaron van den Oord, Yazhe Li, and Oriol Vinyals. Representation learning with contrastive predictive coding. *arXiv preprint arXiv:1807.03748*, 2018. 3
- [44] Jiahong Ouyang, Ehsan Adeli, Kilian M Pohl, Qingyu Zhao, and Greg Zaharchuk. Representation disentanglement for multi-modal brain mri analysis. In *Information Processing in Medical Imaging: 27th International Conference, IPMI 2021, Virtual Event, June 28–June 30, 2021, Proceedings 27*, pages 321–333. Springer, 2021. 2, 3
- [45] Alec Radford, Jong Wook Kim, Chris Hallacy, Aditya Ramesh, Gabriel Goh, Sandhini Agarwal, Girish Sastry, Amanda Askell, Pamela Mishkin, Jack Clark, et al. Learning transferable visual models from natural language supervision. In *International conference on machine learning*, pages 8748–8763. PmLR, 2021. 8, 1
- [46] Olaf Ronneberger, Philipp Fischer, and Thomas Brox. U-net: Convolutional networks for biomedical image segmentation. In *Medical image computing and computer-assisted intervention–MICCAI 2015: 18th international conference, Munich, Germany, October 5-9, 2015, proceedings, part III 18*, pages 234–241. Springer, 2015. 1, 3

- [47] Michael S Ryoo, AJ Piergiovanni, Anurag Arnab, Mostafa Dehghani, and Anelia Angelova. Tokenlearner: What can 8 learned tokens do for images and videos? *arXiv preprint arXiv:2106.11297*, 2021. 2
- [48] Kathryn Schutte, Olivier Moindrot, Paul Hérent, Jean-Baptiste Schiratti, and Simon Jégou. Using stylegan for visual interpretability of deep learning models on medical images. *arXiv preprint arXiv:2101.07563*, 2021. 1, 3
- [49] Dinggang Shen, Guorong Wu, and Heung-Il Suk. Deep learning in medical image analysis. *Annual review of biomedical engineering*, 19(1):221–248, 2017. 1
- [50] Sifan Song, Jinfeng Wang, Qiaochu Zhao, Xiang Li, Dufan Wu, Angelos Stefanidis, Jionglong Su, S Kevin Zhou, and Quanzheng Li. Contrastive learning via equivariant representation. *arXiv preprint arXiv:2406.00262*, 2024. 3
- [51] Fenghe Tang, Lingtao Wang, Chunping Ning, Min Xian, and Jianrui Ding. Cmu-net: a strong convmixer-based medical ultrasound image segmentation network. In *2023 IEEE 20th international symposium on biomedical imaging (ISBI)*, pages 1–5. IEEE, 2023. 2, 6, 7
- [52] Ekin Tiu, Ellie Talius, Pujan Patel, Curtis P Langlotz, Andrew Y Ng, and Pranav Rajpurkar. Expert-level detection of pathologies from unannotated chest x-ray images via self-supervised learning. *Nature biomedical engineering*, 6(12):1399–1406, 2022. 3
- [53] Ashish Vaswani, Noam Shazeer, Niki Parmar, Jakob Uszkoreit, Llion Jones, Aidan N Gomez, Łukasz Kaiser, and Illia Polosukhin. Attention is all you need. *Advances in neural information processing systems*, 30, 2017. 1
- [54] Athanasios Voulodimos, Nikolaos Doulamis, Anastasios Doulamis, and Eftychios Protopapadakis. Deep learning for computer vision: A brief review. *Computational intelligence and neuroscience*, 2018(1):7068349, 2018. 1, 2
- [55] Jie Wang, Chaoliang Zhong, Cheng Feng, Ying Zhang, Jun Sun, and Yasuto Yokota. Disentangled representation for cross-domain medical image segmentation. *IEEE Transactions on Instrumentation and Measurement*, 72:1–15, 2022. 3
- [56] Jinfeng Wang, Sifan Song, Jionglong Su, and S Kevin Zhou. Distortion-disentangled contrastive learning. In *Proceedings of the IEEE/CVF Winter Conference on Applications of Computer Vision*, pages 75–85, 2024. 3
- [57] Shuai Wang and Rui Li. Semantic-guided disentangled representation for unsupervised cross-modality medical image segmentation. *arXiv preprint arXiv:2203.14025*, 2022. 3
- [58] Xin Wang, Hong Chen, Zihao Wu, Wenwu Zhu, et al. Disentangled representation learning. *IEEE Transactions on Pattern Analysis and Machine Intelligence*, 2024. 1, 2, 3
- [59] Alexander D Weston, Panagiotis Korfiatis, Timothy L Kline, Kenneth A Philbrick, Petro Kostandy, Tomas Sakinis, Motokazu Sugimoto, Naoki Takahashi, and Bradley J Erickson. Automated abdominal segmentation of ct scans for body composition analysis using deep learning. *Radiology*, 290(3):669–679, 2019. 1
- [60] Junfei Xiao, Yutong Bai, Alan Yuille, and Zongwei Zhou. Delving into masked autoencoders for multi-label thorax disease classification. In *Proceedings of the IEEE/CVF Winter Conference on Applications of Computer Vision*, pages 3588–3600, 2023. 3
- [61] Taihong Xiao, Jiapeng Hong, and Jinwen Ma. Dna-gan: Learning disentangled representations from multi-attribute images. *arXiv preprint arXiv:1711.05415*, 2017. 2, 3
- [62] Richard Zhang, Phillip Isola, Alexei A Efros, Eli Shechtman, and Oliver Wang. The unreasonable effectiveness of deep features as a perceptual metric. In *Proceedings of the IEEE conference on computer vision and pattern recognition*, pages 586–595, 2018. 5
- [63] Zongwei Zhou, Md Mahfuzur Rahman Siddiquee, Nima Tajbakhsh, and Jianming Liang. Unet++: A nested u-net architecture for medical image segmentation. In *Deep learning in medical image analysis and multimodal learning for clinical decision support: 4th international workshop, DLMIA 2018, and 8th international workshop, ML-CDS 2018, held in conjunction with MICCAI 2018, Granada, Spain, September 20, 2018, proceedings 4*, pages 3–11. Springer, 2018. 2, 3, 6
- [64] Jun-Yan Zhu, Zhoutong Zhang, Chengkai Zhang, Jiajun Wu, Antonio Torralba, Josh Tenenbaum, and Bill Freeman. Visual object networks: Image generation with disentangled 3d representations. *Advances in neural information processing systems*, 31, 2018. 2, 3

OWT: A Foundational Organ-Wise Tokenization Framework for Medical Imaging

Supplementary Material

6. Implementation Details

6.1. Image Preprocessing

For all 3D medical volumes, we standardize the spatial resolution to $2\text{mm} \times 2\text{mm} \times 2\text{mm}$ and apply a center crop of 224×224 . For CT datasets, we clip intensity values to the $[-1000, 1000]$ Hounsfield Unit (HU) range and normalize them to $[0, 1]$. For MRI datasets, we clip intensities to the $[0, 99]$ percentile range and normalize them to $[0, 1]$. We define five token groups to extract semantic features based on common annotations: background, liver, kidneys, spleen, and pancreas. Each medical image is further standardized in thickness by center-padding or cropping 112 slices based on the anatomical centers of the four organs. For the Abdomen1K dataset [40], the number of cases in the training and test sets is 899:101. For AutoPet [21], the split is 700:200, while for RAOS delay and pre-artery sequences [39], both have a training-to-test ratio of 330:83. All experiments, including OWT, MAE, and segmentation networks, are based on the same preprocessed dataset.

For the 2D face images in CelebAMaskHQ dataset [34], we resize them to 224×224 , and define six semantic entities based on annotations (background, face&ear, hair&hat, mouth, nose, and eyes&glasses), as shown in Fig. 8. The CelebAMaskHQ dataset contains 30,000 facial image cases, with 24,000 images allocated for training and 6,000 for testing.

6.2. Architecture Details

6.2.1. Default Architecture of MAE and OWT

In OWT, we adopt the same encoder and decoder architecture as MAE, with the only modification being the replacement of the self-attention blocks [53] with linear self-attention blocks [31]. By default, we use the ViT-base architecture, where the MAE encoder consists of 12 attention blocks, the decoder has 8, and the token embedding dimension is set to 768.

For OWT, we configure the encoder and Token Group Encoder with 6 attention blocks each, while keeping the decoder at 8 blocks. This ensures that the overall model length remains consistent with MAE. Additionally, since each SDTG contains a default of 20 tokens, the computational load of OWT is lower than that of MAE when using fewer than 10 SDTGs. To prevent information leakage during TGR training, we remove the class token from the OWT architecture. For OWT processing 2D images, we use a 16×16 kernel for patch embedding. For 3D input

volumes, we apply a $1 \times 16 \times 16$ 3D kernel for patch embedding.

6.2.2. OWT w/ Text Encoding

For the OWT experiment incorporating text encoding, we design a text prompt inspired by [35]. Specifically, we define the template as "a computerized tomography [category]", where [category] corresponds to "background without the Liver, Kidneys, Spleen, and Pancreas", "of a Liver", "of Kidneys", "of a Spleen", and "of a Pancreas", aligning with the number of token groups. These prompts are fed into a pretrained CLIP text encoder [45] to obtain the corresponding text encoding, resulting in a representation of size 5×512 .

To match the token groups, we replicate each text encoding according to the number of tokens per token group (20), leading to a final text encoding dimension of 100×512 . Within the OWT framework, a linear transformation layer maps the text encoding from 512 to 768, producing a transformed text embedding of size 100×768 . This transformed text encoding is then element-wise added to the organ-wise representation X_G extracted by the Organ Collector. The combined representation proceeds through the random selection procedure in TGR, while all other components remain consistent with the default OWT settings.

6.3. Experimental Setup

We follow the same experimental setup and hyperparameter settings as MAE. Additionally, each MAE- and OWT-based experiment is trained for 1200 epochs, with a 60-epoch warm-up phase. The training follows the learning rate protocol $\text{lr} = \text{base_lr} \times \text{effective_batch_size}/256$ where the base learning rate is set to $\text{base_lr} = 10^{-4}$.

For OWT with 2D image inputs, we set the batch size to 96. When processing 4-slice medical volumes, the batch size is set to 64. In medical imaging training, each unique input (whether a single slice or a 4-slice volume) is treated as an individual input. For instance, a 3D medical volume with a thickness of 112 slices is considered as 112 separate inputs during training. An epoch is defined as the point when all unique inputs in the dataset have been processed once.

For MAE training, we randomly mask 75% of the tokens. During testing, we adjust the mask ratio to 0.25 for improved performance. When MAE is trained with LPIPS loss, all tokens are preserved for image reconstruction.

Abdomen1k	Liver	Kidney	Spleen	Pancreas	Avg Dice \uparrow
UNetplus [63]	96.85	94.63	91.00	71.05	88.38
AttU_Net [42]	97.09	95.22	93.05	72.00	89.34
TransUnet [9]	96.78	94.65	92.30	71.89	88.91
SwinUnet [5]	96.53	93.68	90.52	65.50	86.56
CMUNet [51]	96.05	94.67	90.84	71.75	88.33
OWT	96.55	94.21	95.12	71.32	89.30
OWT/ _{4slices}	96.81	94.84	95.59	78.23	91.37 _{+2.03}

AutoPet	Liver	Kidney	Spleen	Pancreas	Avg Dice \uparrow
UNetplus [63]	96.41	92.56	91.31	76.87	89.29
AttU_Net [42]	96.60	92.86	91.22	78.24	89.73
TransUnet [9]	96.34	93.59	90.65	78.23	89.70
SwinUnet [5]	96.33	92.34	91.11	72.46	88.06
CMUNet [51]	96.56	93.11	90.61	77.65	89.48
OWT	96.14	92.33	92.79	76.82	89.52
OWT/ _{4slices}	96.65	93.15	93.96	81.87	91.41 _{+1.68}

Table 7. Performance of semantic segmentation on CT datasets.

Delay	Liver	Kidney	Spleen	Pancreas	Avg Dice \uparrow
UNetplus [63]	93.53	91.85	85.20	65.85	84.11
AttU_Net [42]	94.25	91.08	86.85	65.98	84.54
TransUnet [9]	93.93	90.83	89.07	66.03	84.97
SwinUnet [5]	92.78	90.61	86.35	62.55	83.07
CMUNet [51]	94.02	91.88	87.74	65.64	84.82
OWT	94.32	91.87	91.55	65.65	85.85
OWT/ _{4slices}	94.72	92.61	92.23	71.33	87.72 _{+1.87}

PreArtery	Liver	Kidney	Spleen	Pancreas	Avg Dice \uparrow
UNetplus [63]	94.05	92.25	87.26	64.14	84.42
AttU_Net [42]	94.33	92.32	89.07	64.45	85.04
TransUnet [9]	94.33	90.69	86.59	65.56	84.29
SwinUnet [5]	92.91	88.91	86.33	61.48	82.41
CMUNet [51]	94.26	92.58	89.21	66.18	85.56
OWT	94.19	91.10	91.82	65.57	85.67
OWT/ _{4slices}	94.74	92.18	92.14	70.17	87.31 _{+1.64}

Table 8. Performance of semantic segmentation on MRI datasets.

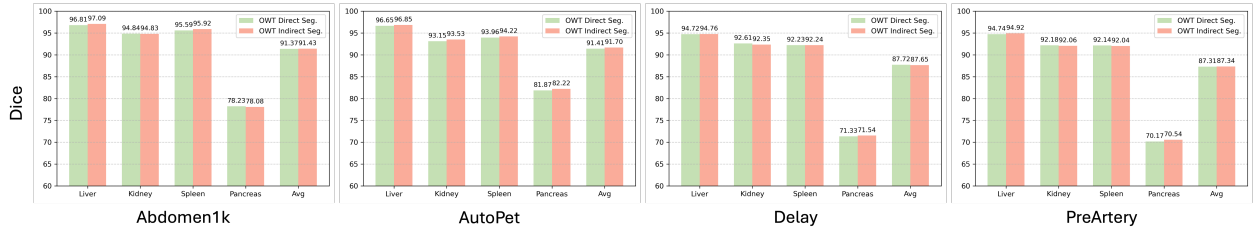


Figure 10. Comparison of segmentation performance using direct and indirect approaches.

All reconstructed images are filtered with a 0.02 pixel-range threshold to reduce background noise. For the interpretability experiments validated by segmentation, we apply a 0.15 threshold to transfer the reconstructed results as semantic masks.

7. Detailed Semantic Segmentation Results

Detailed Results. Tables 7 and 8 provide a more detailed results of those presented in Table 3, showing the Dice scores for each of the four organs across different datasets. From Tables 7 and 8, we observe that compared to dedicated segmentation networks, OWT/_{4slices} generally achieves superior performance across all organs. Notably, for smaller organs such as the pancreas, OWT/_{4slices} demonstrates a significant improvement, with a Dice score advantage exceeding 5.3 in the best case.

Token Group Connectivity. For semantic segmentation using OWT, we generate masks by processing independently utilized Semantically Disentangled Token Groups (SDTGs) through the Token Group Encoder, AHER, and decoder to reconstruct an image, which is then thresholded to produce a segmentation mask. We refer to this mask as the “direct” mask. Since SDTGs can be flexibly combined, we also explore an alternative approach: subtracting the reconstructed images from all other four SDTGs from the input image and applying a threshold to obtain a predicted mask for the same organ. We define this as the “indirect”

Method	AutoPet		CelebAMaskHQ	
	L2 \downarrow	LPIPS \downarrow	L2 \downarrow	LPIPS \downarrow
MAE/LPIPS	2.77e-04	0.0255	2.78e-03	0.1157
OWT	1.49e-04	0.0232	2.50e-03	0.1101
OWT/VQGAN	6.89e-05 _{↓53.8%}	0.0073 _{↓68.5%}	1.80e-03 _{↓43.8%}	0.0540 _{↓51.0%}

Table 9. Performance comparison when altering the Transformer-based encoder and decoder to those of VQGAN.

mask.

Although using all complementary SDTGs reduces computational efficiency compared to single SDTG usage, it incorporates additional inter- and intra-organ information, potentially enhancing connectivity in the segmentation process. To evaluate whether leveraging more SDTGs improves boundary and shape reconstruction, we conduct comparative experiments. The results, presented in Fig. 10, show that across four datasets, the direct and indirect methods yield largely similar outcomes. This demonstrates that the SDTGs extracted by OWT maintain a high degree of semantic independence, as they accurately capture organ boundaries and shapes even when used independently. These findings align with the t-SNE visualization of SDTG relationships in Fig. 6, further validating their disentangled nature.

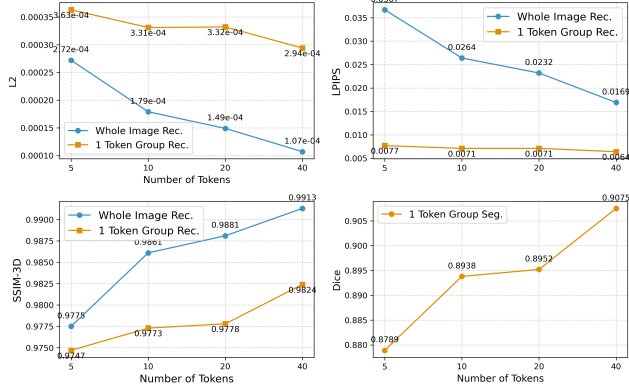


Figure 11. Ablation study on the number of tokens in each token group when trained on AutoPet.

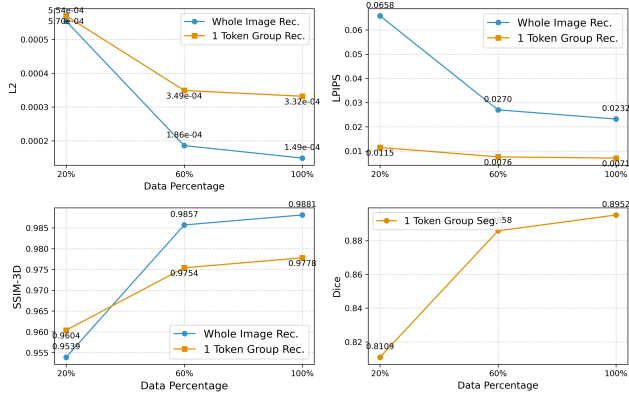


Figure 12. Ablation study on OWT performance when utilizing different percentages of the dataset (AutoPet).

8. Ablation Studies

For the ablation study, we explore the following key aspects: the flexibility of the encoder-decoder architecture, the number of tokens per SDTG, and the impact of varying the amount of input data in OWT.

Backbone Alteration. We investigate the effect of replacing the default ViT-based encoder-decoder architecture in OWT (adopted from MAE) with the encoder and decoder from VQGAN. Specifically, we configure the VQGAN bottleneck dimensions to 14×14 for a 224×224 input image, ensuring that the number of latent tokens (196) remains consistent with the ViT-based setting. As shown in Table 9, despite the increased computational cost of VQGAN’s hybrid CNN and self-attention structure, it achieves significant performance gains over the transformer-based encoder-decoder. On two (medical and facial) datasets, it improves both L2 and LPIPS evaluation metrics by 43.8%–68.5%, demonstrating the potential for further enhancements in OWT and highlighting its architectural flexibility.

Number of Tokens per SDTG. The number of tokens within each SDTG determines its capacity to store organ-specific information. To evaluate this, we experiment with SDTG token counts of 5, 10, 20, and 40, assessing their impact on both generation and segmentation tasks. For the generation task, we measure full-image reconstruction using all SDTGs and single-organ reconstruction using only one SDTG, evaluated by L2, LPIPS, and SSIM-3D metrics. For segmentation, we assess the Dice score of single-organ masks.

As shown in Fig. 11, increasing the token count from 10 to 20 provides a slight performance improvement, while further increasing it from 20 to 40 leads to a more significant boost. This suggests that OWT has considerable scalability and potential as a foundational semantic-level tokenization framework, capable of further enhancements with increased token capacity.

Data Percentage. Fig. 12 illustrates the performance of the OWT framework on the AutoPet dataset when trained with 20%, 60%, and 100% of the data. We observe a significant improvement in performance when increasing the dataset size from 20% to 60%, whereas the gain from 60% to 100% is relatively marginal. This suggests that OWT efficiently learns meaningful representations with a moderate amount of data, indicating its strong data efficiency and the potential for effective generalization even with limited training samples.